communications biology

ARTICLE

https://doi.org/10.1038/s42003-021-02903-7 OPEN

Cooperative allostery and structural dynamics of streptavidin at cryogenic- and ambient-temperature

Esra Ayan[1,11], Busra Yuksel[1,11], Ebru Destan[1,11], Fatma Betul Ertem[1], Gunseli Yildirim[1], Meryem Eren[1], Oleksandr M. Yefanov[2], Anton Barty[2], Alexandra Tolstikova[2], Gihan K. Ketawala[3,4], Sabine Botha[3,4], E. Han Dao[5], Brandon Hayes[6], Mengning Liang[6], Matthew H. Seaberg[6], Mark S. Hunter[6], Alexander Batyuk[6], Valerio Mariani[6], Zhen Su[6,7], Frederic Poitevin[6], Chun Hong Yoon[6], Christopher Kupitz[6], Aina Cohen[8], Tzanko Doukov[8], Raymond G. Sierra[6], Çağdaş Dağ[1,9,10] & Hasan DeMirci[1,5,10]✉

Multimeric protein assemblies are abundant in nature. Streptavidin is an attractive protein that provides a paradigm system to investigate the intra- and intermolecular interactions of multimeric protein complexes. Also, it offers a versatile tool for biotechnological applications. Here, we present two apo-streptavidin structures, the first one is an ambient temperature Serial Femtosecond X-ray crystal (Apo-SFX) structure at 1.7 Å resolution and the second one is a cryogenic crystal structure (Apo-Cryo) at 1.1 Å resolution. These structures are mostly in agreement with previous structural data. Combined with computational analysis, these structures provide invaluable information about structural dynamics of apo streptavidin. Collectively, these data further reveal a novel cooperative allostery of streptavidin which binds to substrate via water molecules that provide a polar interaction network and mimics the substrate biotin which displays one of the strongest affinities found in nature.

[1] Department of Molecular Biology and Genetics, Koc University, 34450 Istanbul, Turkey. [2] Deutsches Elektronen-Synchrotron, Notkestrasse 85, 22607 Hamburg, Germany. [3] Department of Physics, Arizona State University, Tempe, AZ 85287-1504, USA. [4] Biodesign Center for Applied Structural Discovery, Arizona State University, Tempe, AZ 85287-5001, USA. [5] Stanford PULSE Institute, SLAC National Laboratory, Menlo Park, CA 94025, USA. [6] Linac Coherent Light Source, SLAC National Accelerator Laboratory, 2575 Sand Hill Road, Menlo Park, CA 94025, USA. [7] Department of Applied Physics, Stanford University, Stanford, CA 94305, USA. [8] Stanford Synchrotron Radiation Lightsource, SLAC National Accelerator Laboratory, 2575 Sand Hill Road, Menlo Park, CA 94025, USA. [9] Nanofabrication and Nanocharacterization Center for Scientific and Technological Advanced Research, Koc University, 34450 Istanbul, Turkey. [10] Koc University Isbank Center for Infectious Diseases (KUISCID), 34010 Istanbul, Turkey. [11] These authors contributed equally: Esra Ayan, Busra Yuksel, Ebru Destan. ✉email: hdemirci@ku.edu.tr

Core streptavidin is a biotin-binding protein and has a homotetrameric structure consisting of 126 amino acid residues in each identical monomer[1]. The secondary structure of streptavidin involves the formation of an anti-parallel eight-stranded β-barrel tertiary structure[2]. Trp120 residue in each monomer is responsible for the linkage of the monomer to its neighboring subunits. Tetramers can be seen as composed of two functional dimers[3]. Although the function of streptavidin is not well known, previous studies suggest that streptavidin may play a role in microbial defense mechanisms[4].

For many years, the strong non-covalent bond between biotin and streptavidin has attracted the attention of scientists in basic and applied sciences. Theoretically, the strength of streptavidin–biotin conjugation is known by its pinpoint specification and femtomolar affinity ($K_d = 10^{-13}$–10^{-15} M)[5]. This affinity is an order of magnitude higher than prominent antigen–antibody interactions[6]. This specific affinity of the streptavidin–biotin complex contains remarkable properties. First, there is a high shape-complementarity between the binding pocket and biotin, and this affinity is strengthened by hydrogen bonds with specific residues, i.e. Asn23, Ser42, Tyr43, Ser45, Asn49, Ser88, Thr90, and Asp128[7]. Additionally, in the hydrophobic binding pocket, numerous Van der Waals contacts with biotin make this one of the strongest non-covalent interactions with molecular dynamics studies highlighting the non-polar Van der Waals contribution of tryptophan residues, e.g., Trp79, Trp92, Trp108, and Trp120, rather than electrostatic forces[3,8,9]. Protein regions which are involved in protein-protein and protein-target interactions have high plasticity and are often highly flexible. In addition, these regions are usually located on the solvent exposed surface of the protein. Apo-state streptavidin loop (L3/4; residues 45–52) (Supplementary Fig. 1) is the crucial segment of streptavidin that interacts with biotin and regulates binding action[10].

Previous studies have contributed significantly to our discovery-based knowledge about the streptavidin–biotin structure (Supplementary Fig. 2) and provided innovations in biotechnology, including a drug delivery method and catalysis and detection and labeling of molecules[11–15]. Furthermore, streptavidin provided numerous pragmatic platforms as a tool for orienting and delivering signals from proteins[16]. New applications are added continually to develop new organic nanomolecules. The structural dynamics of streptavidin and its interactions with small molecules demonstrate that we have a greater understanding of its structure-function relationship, which makes it an easy to "plug and play" type of molecule[15]. Streptavidin is a molecule characterized by its interactions with a wide range of biotinylated molecules and is widely used in biotechnology. Its binding with biotinylated molecules is diffusion-limited and has a remarkably high binding efficiency. Streptavidin can form new nano-assemblies by using biotinylated non-biological building blocks as well as organic molecules such as sugar, protein, and nucleic acids[15]. Tetrameric streptavidin displays non-symmetrical subunit structures in the L3/4 region. The mutated residues (N23A/S27D/S45A) favor the open conformation of the L3/4 and further decrease the biotin-binding affinity[17]. Engineered divalent *cis*- and *trans*-plane-dependent streptavidin demonstrated that the overlay of wild-type and the mutated residues may also cause a decrease in the number of polar linkages interacting with biotin[14]. These mutated residues offer a potential target for further modulating streptavidin properties.

There are conflicting hypotheses on the cooperativity of the streptavidin–biotin interaction. Some suggest that these interactions are cooperative[18,19] while others suggest noncooperative binding based on the holo- and apo-streptavidin–biotin complexes[20]. Along with two opposing views, it was also suggested that the streptavidin–biotin interaction showed positive cooperativity, and the cooperativity of the tetramer was accompanied by closeness of the streptavidin upon biotin binding[21,22]. Later on, this phenomenon was named "cooperative allosterism"[23]. Streptavidin–biotin complex has numerous applications and many of them are investigated structurally. There are existing cryogenic apo-state structures in the literature[24]; however, temperature artifacts could introduce errors, preventing successful computational predictions[25]. In addition, cryogenic temperature may perturb the overall protein backbone fold[26]. Therefore, studies have recommended greater caution when referring only to cryogenic structures[24,25]. In order to reveal the underpinnings of this elegant system, it is essential to examine the details of structural dynamics of the apo-state at near-physiological temperatures, which are currently a missing reference point.

Streptavidin structure at ambient temperature will provide further information to explore the structural dynamics of this protein in more detail (Supplementary Fig. 2). We obtained the radiation-damage-free ambient temperature Apo-SFX structure of streptavidin at 1.7 Å resolution during the first ever remote data collection at the Macromolecular Femtosecond Crystallography (MFX) instrument at Linac Coherent Light Source (LCLS)[27]. The diffraction data are collected by using the new generation ePix10k2M detector, which has a much improved dynamic range and lower noise than the previous family of detectors[28] (Supplementary Fig. 3). In addition to our Apo-SFX structure, we also present Apo-Cryo structure at 1.1 Å resolution for structural comparison. We re-evaluated the tetrameric structure of streptavidin by Gaussian Network Model (GNM) analysis of the protein's dynamics[29] by inspecting the Apo-SFX and Holo-SFX (PDB ID: 5JD2) structures. The new Apo-SFX structure, which has higher resolution and improved electron density quality compared to previous ambient temperature apo-structures, and Holo-SFX structure were determined from data collected at the same X-ray source. Thus, temperature- and instrument-related differences and variables are minimized within these structures for accurate comparison in GNM analysis. To highlight the structural dynamics of streptavidin, we investigated the polar interaction network, number of coordinated water molecules, thermal ellipsoid structures, and electrostatic surface models for both ambient and cryogenic structures. Our data presented here provide a novel cooperative allosteric model for streptavidin–biotin interactions.

Results

Ambient-temperature X-ray free-electron laser (XFEL) and cryogenic synchrotron structures of streptavidin revealed alternate conformations of the binding pocket. We determined the first radiation-damage-free SFX crystal structure of apo-streptavidin at 1.7 Å resolution (Fig. 1a, b and Table 1). The diffraction data were collected during the first remote beamtime at the MFX instrument of the LCLS at SLAC National Laboratory, Menlo Park, CA[27]. The second crystal structure of apo-streptavidin was determined at a 1.1 Å resolution at cryogenic temperatures at beamline 12-2 of the Stanford Synchrotron Radiation Lightsource (SSRL) in Menlo Park, CA (Supplementary Fig. 4a–c and Table 1). Subunits of the two tetrameric crystal structures at ambient and cryogenic temperatures were superposed with an overall root-mean-square deviation (RMSD) of 0.17 and 0.13 Å, respectively (Fig. 1c and Supplementary Fig. 4c). Conformational changes were observed around the loop regions of these monomers.

Superposition of our Apo-SFX and Apo-Cryo structures revealed very similar conformations of the substrate-binding

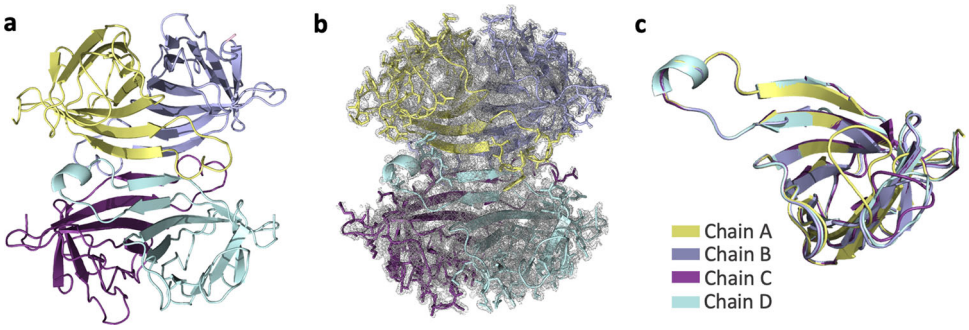

Fig. 1 Apo-SFX structure of streptavidin. a The Apo structure of streptavidin is colored based on each chain. **b** 2*Fo*-*Fc* simulated annealing-omit map at 1 sigma level is colored in gray. **c** Each chain of streptavidin is superposed with an overall RMSD of 0.177 Å.

Table 1 Data collection and refinement statistics.

	Apo-SFX Streptavidin	Apo-Cryo Streptavidin[a]
Data collection	PDB ID (7EK8)	PDB ID (7EK9)
Instrument	LCLS (MFX)	SSRL (BL12-2)
Space group	$P12_11$	$P12_11$
Cell dimensions		
a, *b*, *c* (Å)	47.40, 87.70, 58.90	46.36, 85.76, 58.13
α, *β*, *γ* (°)	90.00, 98.90, 90.00	90.00, 98.71, 90.00
Resolution (Å)[b]	48.49–1.70 (1.76–1.70)[c]	17.89–1.1 (1.14–1.10)
R_{split}	11.02 (77.82)	—
R_{pim}	—	0.045 (0.30)
R_{meas}	—	0.058 (0.35)
CC1/2	0.98 (0.61)	0.58 (0.77)
$I/\sigma(I)$	8.91 (1.10)	14.45 (2.72)
CC*	0.99 (0.87)	0.98 (0.93)
Completeness (%)	100.0 (100.0)	80.70 (47.8)[b]
Redundancy	897 (63)	2.1 (1.7)
Refinement		
Resolution (Å)	48.49–1.70 (1.74–1.70)	17.89–1.10 (1.11–1.10)
No. of reflections	52,270 (3572)	147,223 (2405)
R_{work}/R_{free}	0.19/0.22 (0.37/0.36)	0.16/0.19 (0.22/0.24)
No. of atoms		
Protein	3769	3855
Ligand/ion	397	624
B-factors		
Protein	18.14	18.65
Ligand/ion/water	34.42	33.82
Coordinate errors	0.21	0.09
R.m.s. deviations		
Bond lengths (Å)	0.011	0.012
Bond angles (°)	1.058	1.345
Ramachandran plot		
Favored (%)	98.31	97.47
Allowed (%)	1.48	2.11
Disallowed (%)	0.21	0.42

[a]One crystal was used for the Apo-Cryo Streptavidin dataset. Multiple crystals were used for the Apo-SFX dataset.
[b]Completeness of Apo-Cryo Streptavidin dataset is 86.7 at 1.18 Å.
[c]The highest resolution shell is shown in parenthesis.

sites with an overall RMSD of 0.30 Å (Fig. 2a–d and Supplementary Table 1). We observed additional electron density that belongs to the residues in the ligand-binding site region, which were not modeled in previous studies (Fig. 1a–c and Supplementary Figs. 4a–c, 5, and 6). First, we compared the ambient temperature synchrotron apo-structure of streptavidin (1SWB) with our Apo-SFX structure[30]. 1SWB was determined at 1.85 Å resolution with an R_{work} of 0.17 and R_{free} of 0.25 while the Apo-SFX structure was determined at 1.7 Å resolution with an R_{work} of 0.19 and R_{free} of 0.22. The 1SWB structure has missing residues in chain B at positions 45–48, and in chain C and D at positions 46–48, as mentioned in Supplementary Fig. 5. Moreover, 1SWB was observed with lack of electron density at residues Gln24, Lue25, Val47, Glu51, and Arg53 in different chains, thus this structure was not suitable for applying GNM analysis. Moreover, for a fair comparison, we compared the electron density of binding site residues between our Apo-SFX structure and the latest synchrotron cryo-structure of apo-streptavidin (PDB ID: 3RY1)[31] and found that the electron density of the loops, unfortunately, was not enhanced significantly (Supplementary Fig. 6). Overall, 3RY1 was determined at 1.03 Å resolution, while Apo-SFX was determined at a lower resolution. On the other hand, in our Apo-SFX data, some of the binding site residues' electron density enhanced, and continuous electron density without alternate side-chain conformations was observed. In particular, chain A within the Apo-SFX structure between Ile30-Thr40, Ala46-Arg53, and Glu44 have clearer electron density and precise side-chain conformations compared to the 3RY1 structure as indicated in the following figure. In chain B, between Asn23-Gly26, Phe29-Leu39, Ser45-Gly48, Glu51-Val55, and Thr42 there is more precise electron density and a lack of alternate side-chain conformations for the Apo-SFX structure. In chain C Asn23-Leu25, Ile30, The32, Ala35, Glu44, and Glu51 have clearer and continuous electron density with less alternate conformations within the Apo-SFX structure; however, between Ala46-Ala50 and Arg53, the electron density is clearer at 3RY1 but has similar conformations to Apo-SFX. Similarly, in chain D the Apo-SFX structure has a clearer density and more precise conformations for Asn23-Leu25, Ile30, The32, Ala35-Ala38 (but not Asp36), and Thr42; however, for Glu44-Ser52 the 3RY1 structure has clearer electron density but similar conformations to Apo-SFX.

The non-covalent interactions between biotin and streptavidin in the binding pocket residues (Asn23, Ser27, Tyr43, Ser45, Asn49, Ser88, Asp128) play an essential role in making the structure more stable[7]. To explore the noncovalent interactions in the binding pocket, hydrogen bonds were mapped between the active site and neighboring residues (Supplementary Fig. 7a, b). In doing so, the superposition of Apo-SFX and Apo-CryoEM (PDB_ID:6J6K) structures revealed the differences between the substrate-binding pocket residues (Supplementary Fig. 8a–d and Supplementary Table 1). Especially the residues Ser45 and Asn49 around the L3/4 region showed significant conformational differences. These residues are important for the noncovalent interactions with a biotin substrate. Interestingly, this conformational change is more prominent for chains B–D. Conformational differences of L3/4 indicate the non-symmetric binding of biotin

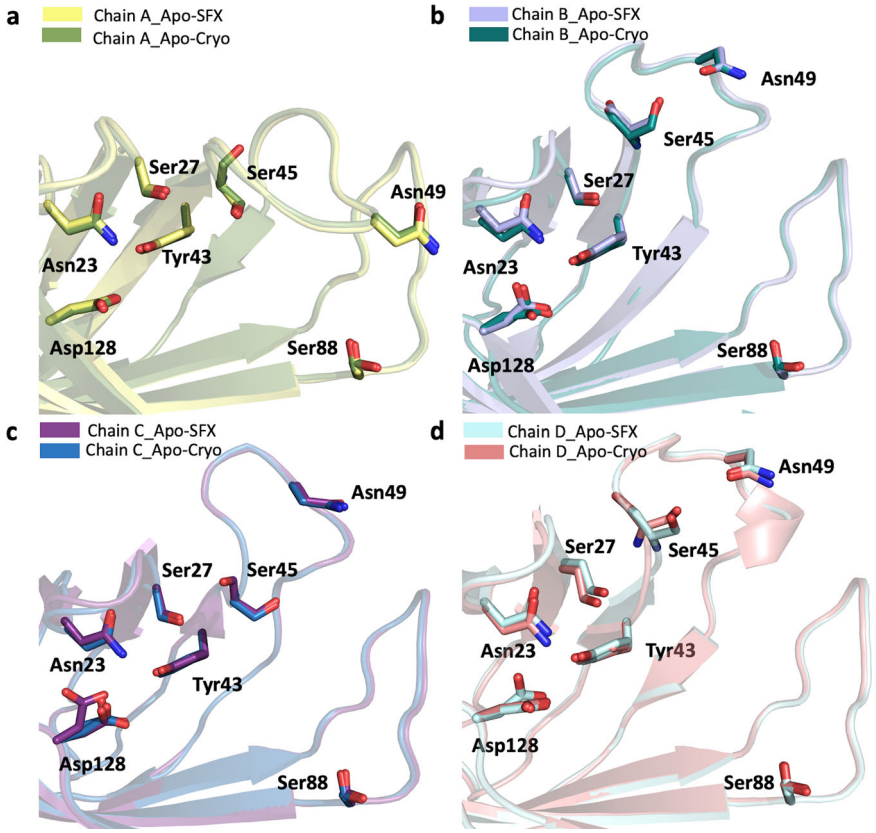

Fig. 2 Biotin-binding site comparison of Apo-SFX and Apo-Cryo structures of streptavidin. Chains A–D of Apo-SFX is superposed with Apo-Cryo structure in **a**–**d**, respectively (Supplementary Table 1). There are no significant conformational differences between the two structures.

with monomers (Supplementary Fig 9a–d). The superposition of our Apo-SFX structure was performed by using the Holo-CryoEM structure (PDB ID: 6J6J; Supplementary Fig. 9a–d and Supplementary Table 1) and Holo-SFX structure (Supplementary Fig. 10a–d, Fig. 3a–d, and Supplementary Table 2). Additionally, we superposed Apo-Cryo structure with the Holo-SFX structure (Supplementary Fig. 11a–d and Supplementary Table 2). As expected, conformational changes were found in the binding pocket. Furthermore, we observed the minor conformational changes that are <1 Å at the residues Ala65, Thr66, Asp77, Ala100, Glu101, Glu116, Ala117, Asp128, Lys132, Val133, and Lys134 correlated with previous mutation studies to elucidate its dynamic application[19,32–35] (Supplementary Fig. 12a–d).

To provide more detailed information about the binding pocket conformation and interactions of streptavidin in all three structures (Supplementary Fig. 13a–c), water molecules around the binding pocket of each chain were investigated (Fig. 4a–c). Apo structures have a wider opening for ligand binding at B–D chains compared to the Holo-SFX structure. On the other hand, chain A displayed disrupted symmetry and an alternate conformation with a closed state similar to the Holo-SFX conformation (Fig. 4a–c). Moreover, our data reveal that chain A, which has the highest number of coordinated water molecules, that interact with binding pocket residues, favors the closed state of the flexible loop due to polar interactions. Similarly, the open-loop conformation correlates with a gradually reduced number of coordinated water molecules and polar contacts in the binding pocket (Fig. 5a–d). Our data suggest that coordinated water molecules in the binding pocket and polar interaction network have a key role in cooperativity.

To determine the structural dynamics of each subunit together, temperature factor analysis was performed and compared with the Holo-SFX structure (Fig. 6a–c). While the two crystal structures of streptavidin reveal an inelastic binding pocket for chains A and B, we observed more intrinsic plasticity, especially in the loop region around the binding pocket of chains C and D. Electrostatic forces carry significant importance for protein–protein interactions and protein stability. The biotin-binding pocket for each chain was surrounded by a basic region concentrated with positively charged residues (Fig. 7a–c). These surface charge redistributions can cause shape perturbations of a protein by altering hydrogen bonds and salt bridges.

GNM analysis. The GNM analysis is a coarse-grained Normal Mode Analysis method that is efficient in revealing a protein's dynamics[36]. The normal modes obtained describe the microstates accessible to the protein's native state. The theoretical fluctuations calculated with normal modes from GNM correlate with the thermal fluctuations found in X-ray experimentation as well. Slow modes have the highest mode weights and contain the most collective residue motions. These are the intrinsic fluctuations required for the protein's global motion[37]. Therefore, Apo-SFX and Holo-SFX structures were analyzed with GNM to compare the apo- and holo-state streptavidin dynamics thoroughly. Cross-correlations between residue motions were investigated and mean squared fluctuations that describe the flexibility of the residues were analyzed. The theoretical fluctuations calculated from all modes were aligned to the B-factors in Supplementary Fig. 14a, b. They showed high correlation at the selected cut-off distance of 7.3 Å: overall correlation with *B*-factors was 0.785 in the GNM of Holo-SFX structure and 0.646 in the GNM of Apo-SFX structure. Cross-correlations between residue motions were investigated across all different modes in order to inspect the communication

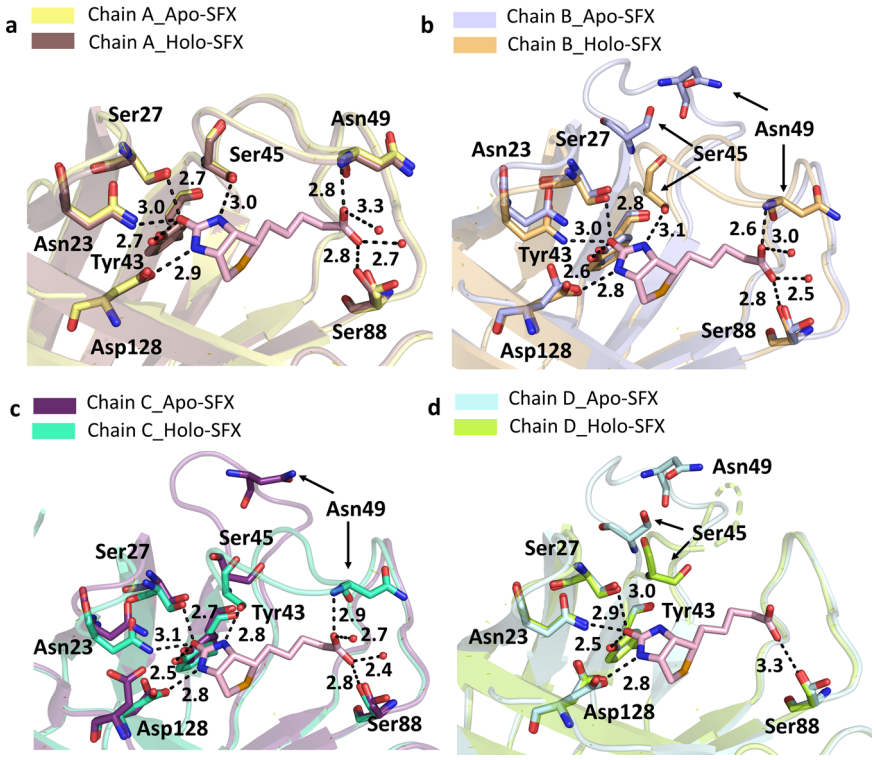

Fig. 3 Superposition of the biotin-binding sites for each chain of the Apo-SFX and Holo-SFX structures. Chains A–D of Apo-SFX is superposed with the Holo-SFX (PDB ID:5JD2) structure of streptavidin in **a**–**d**, respectively (Supplementary Table 1). The L3/4 opening as a "lid" without selenobiotin binding. Binding of selenobiotin is not symmetric for all four monomers, which represent cooperativity. Selenobiotin and water molecules were represented by light pink sticks and red-colored spheres, respectively. Hydrogen bonds are shown with black dashed lines and their corresponding distance as a unit of Angstrom (Å).

in the residue networks. Accordingly, chains A and B and chains C and D were observed as dimers with highly correlated motions in both Apo-SFX and Holo-SFX structures (Fig. 8a, b). The active site residues of the Holo-SFX structure and selenobiotin ligand interactions of the related chains showed highly correlated motions as expected (Fig. 8a). The intrachain residues' cross-correlation section further showed that the first 50 residues had highly correlated motions. These residues belong to the same β-sheet with an extensive H-bond network. Moreover, residues after the 127th are highly correlated with those of the intrachain sections in both Apo-SFX and Holo-SFX structures (Fig. 8a, b). Remarkably, correlated motion was especially high between 23–30th and 96–110th positions and between 83–84th and 49–51st positions, respectively. Besides, residues in Trp120-Asp128 showed correlated motion with same numbered residues of the associated chain on the other dimer for both the Apo-SFX and Holo-SFX structures (Fig. 8a, b). The result is expected due to Trp120 creating a water channel with Asp128 for the removal of waters from the streptavidin-binding pocket, thus enhancing ligand binding[18]. The interchain cross-correlation sections within the dimers show highly correlated motions between residues Thr57 and Arg59, Thr71 and Lys80, His87 and Ser93, and Leu110 and Gly113. Similarly, Asp61 has correlated motion between residues Thr76 and Thr90 of the neighboring chain on the same dimer (Fig. 8a, b).

Cross-correlation differences between selected chains of Apo-SFX and Holo-SFX structures were also evaluated (Fig. 8c, d). In these heat-maps, red indicates an increase in correlated motion between residues relative to the Apo-SFX structure, and blue means a decrease. Accordingly, when comparing the same chain of the two structures, residues between 45 and 51 have a higher correlation with residues 86–93, 110–114, and 121–129 within the Holo-SFX streptavidin than Apo-SFX streptavidin (Fig. 8c). Moreover, in the Holo-SFX structure, Ile17 and Val31, Ala35 and Ala38, Ser45 and Glu51, and Thr57 and Arg59 displayed higher correlated motion when compared to Apo-SFX streptavidin. Furthermore, Apo-SFX streptavidin residues Gly26, Ala46 and Trp120 have higher correlation with all residues relative to the Holo-SFX structure (Fig. 8c). In particular, correlation of Gly26 with residues between 129 and 134 decreased for the Holo-SFX structure (Fig. 8c). On the other hand, correlation differences between the Apo-SFX and Holo-SFX structure of streptavidin are also different across chains in the same dimer (Fig. 8d). Interestingly, binding site residues have a higher correlation overall with residues of the opposite chain in Apo-SFX; correlation is highest with residues in position 16–40, 59–74, and 95–110 (Fig. 8d). In addition, Trp120 showed decreased correlation with residues of the opposite chain in the same dimer relative to Holo-SFX streptavidin (Fig. 8d).

Global protein motions were inspected closer to further determine the effects of selenobiotin binding on intrinsic residue fluctuations. Specifically, the mean squared fluctuations of the 10 slowest modes were obtained (Fig. 8e). These fluctuations reveal the protein's global motion. Accordingly, fluctuation profiles of each chain demonstrate that regional flexibility contributes to the global motion of streptavidin. Thereafter, the Apo-SFX structure was observed with higher fluctuations around the selenobiotin-binding site. Moreover, chains A–D showed increased flexibility, especially in the selenobiotin-binding site, as evidenced by the high residue fluctuations. This result suggests that residues within L3/4, adjacent to the binding site, are intrinsically disordered and transitioning in between closed and open conformations in the absence of the ligand. Besides, the presence of selenobiotin binding with streptavidin was observed

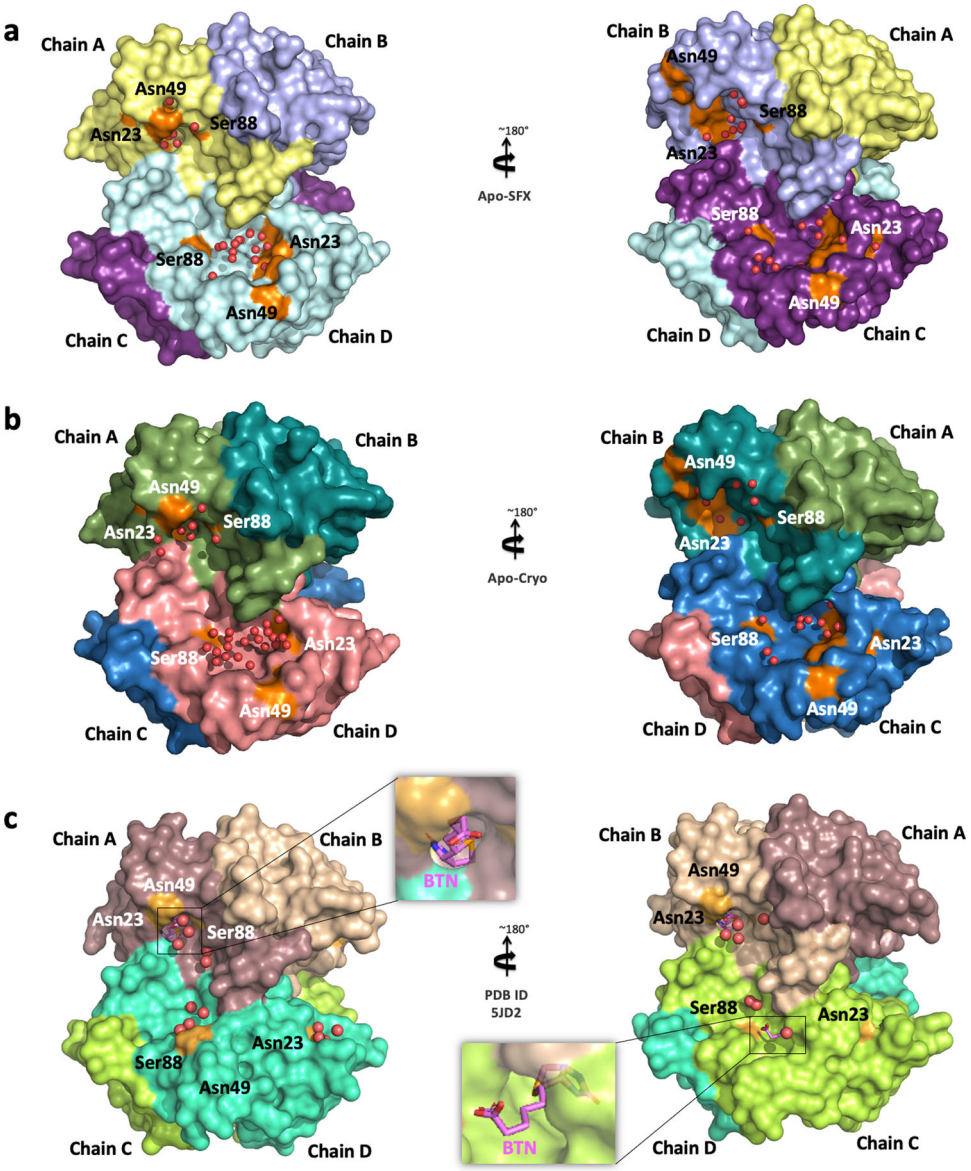

Fig. 4 Representation of water molecules in the binding pocket of streptavidin structures. a Apo-SFX structure and **b** Apo-Cryo structure of apo-state streptavidin and **c** Holo-SFX structure with selenobiotin (BTN) (PDB ID: 5JD2) are shown with their surface and water molecules are shown with red spheres. The indicated residues around the binding pocket are shown in orange color.

with higher fluctuations around the 66, 110, and 116th residues. It must be noted that disordered residues were observed in chain D of the Holo-SFX structure at L3/4 (Fig. 3d), which also can be clearly seen from the GNM analysis graph (Fig. 8e). Additionally, although the conformations should be similar in Apo-SFX chain A for both structures, fluctuation differences were observed between the structures' binding sites.

Discussion

The quaternary structures represent the highest complexity state in the structural hierarchy. The assembly of subunits interacting via noncovalent and covalent bonds determine their structure–function correlations[38]. Oligomeric proteins are presumed to be more robust and have evolutionary advantages over monomeric ones[39,40]. The prevalence of proteins with a quaternary structure in biological systems is closely related to cooperativity[41]. There is no certain theoretical definition of this cooperativity in enzymology. The tetrameric structure of streptavidin is known as having the strongest binding affinity found in nature to its substrate biotin and it may thus further contribute to the understanding of cooperativity[18,34,42]. Simultaneous binding of four biotin ligands to streptavidin with full occupancy is unlikely[14]. Our previous structure of tetrameric Holo-SFX also displayed comparable properties with partial binding of selenobiotin to chain D[43]. In GNM analysis, the interchain residues displayed correlated motions with neighbor residues in the same dimers. Moreover, binding site residues generally have higher correlations with residues of the opposite chain (especially between 16–40th, 59–74th, and 95–110th residues) in the Holo-SFX structure. In addition, Trp120 of the Apo-SFX structure had a higher correlation with overall residues than the Holo-SFX structure. This may confirm that the apo form of streptavidin displays tetrameric cooperativity via Trp120. Besides, biotin binding stabilizes the L3/4 of streptavidin in tetrameric form, which can be observed with lower fluctuations (Fig. 8e). However, there are increased fluctuations such as Trp120 that are important for interchain connection within the tetramer (Fig. 8e). Although a previous study indicated that the binding of biotin is not

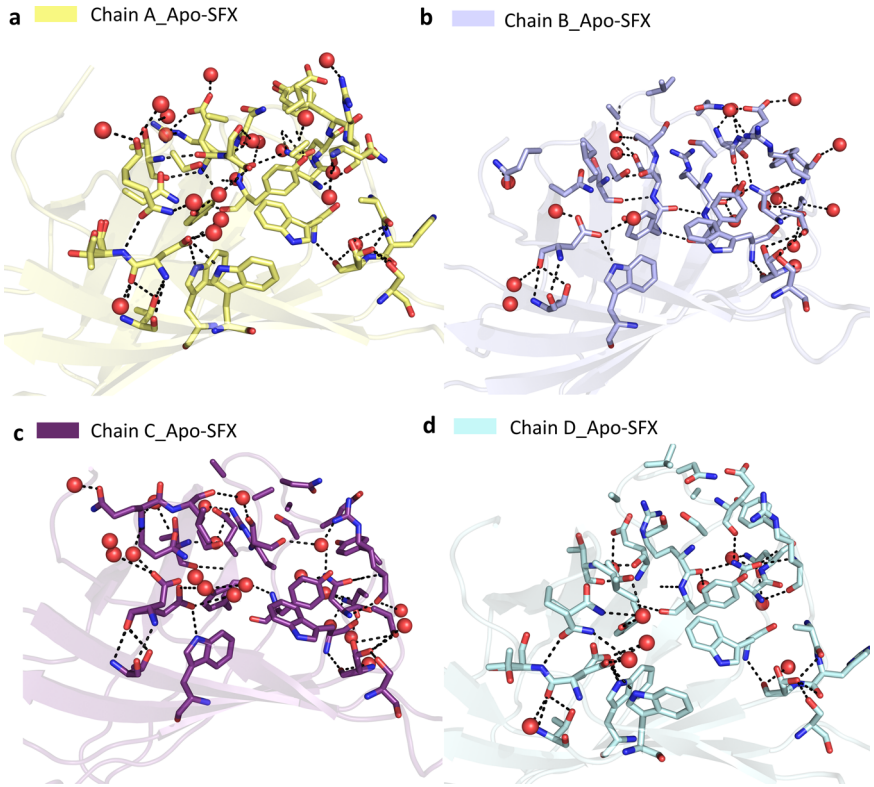

Fig. 5 Representation of coordinated water molecules and polar interactions near the binding sites for each chain of Apo-SFX structure. Coordinated water molecules within the binding pocket were altered and polar interactions were reduced with loop opening in Apo-SFX structure. All polar interactions were observed within 3.6 Å. **a** Binding site residues of chain A were observed with 19 water molecules and 51 polar interactions. Those interactions provide the stability of the chain, which was similar to the selenobiotin-bounded structure. **b** Chain B-binding site residues were determined with 19 water molecules and 46 polar interactions that were involved. **c** Residues of the binding site of chain C have 40 polar interactions between residues and 20 water molecules. **d** Chain D-binding site residues involve 9 water molecules and 31 polar interactions. All interactions included H-bonds and electrostatic interactions and are presented with dashed lines. Water molecules are indicated with red-colored spheres.

cooperative according to principal component analysis[44], these results confirm that biotin binding may not have a stabilizing effect but can cause the allosteric response of streptavidin[23]. Also, biotin binding may affect other dimer chains of the tetrameric structure and provide cooperativity for additional ligand binding by perturbing active site residues.

In this study, we examined the polar interaction network of each subunit of the tetrameric Apo-SFX structure (Fig. 5a–d). We compared the binding sites of the Holo-SFX structure with the Apo-SFX structure (Fig. 3a–d). L3/4 helps ligand binding by removing excessive solvent, which destabilizes H-bond interactions of the active site with a ligand. The free energy increase of 27.1 kcal/mol from the open to closed state transition of L3/4 was indicated[42]. It has been demonstrated that the open conformation of L3/4 is more favorable than the closed conformation[42]. This suggests that the "lid" closing is not spontaneous; however, the opening is spontaneous because of a lack of stabilization of an extensive polar interaction network with biotin. As a driving force, the closing of the lid may be caused by the allosteric and cooperative "pump-like" motions of tetrameric streptavidin which forcibly removes excessive water molecules from the ligand binding site. This model is consistent with a previous study which indicated biotin dissociation is initiated by water entry and weakening H-bonds between binding site residues and biotin[18]. This may suggest cooperativity of a tetrameric form providing a higher affinity due to the removal of excess water molecules for establishing an extensive H-bond network in the binding pocket.

Open-loop conformation of the Apo-SFX streptavidin structure was supported with a *B*-factor analysis and represented as an ellipsoid model[45] (Fig. 6a–c). Based on GNM results, the L3/4 was observed with higher fluctuations in Apo-SFX streptavidin, representing higher mobility of the residues (Fig. 8e). One reason for the striking difference in fluctuations is that selenobiotin was included in the GNM of Holo-SFX (5JD2) and therefore the ligand's effect on decreasing the flexibility of the region was more clear in the protein's global motions. The tetrameric form of the enzyme is the most efficient form of the streptavidin–biotin complex when compared to dimeric and monomeric forms[14]. Interestingly, we observed higher correlated motions of residues in dimers, which may indicate dimeric cooperativity of the streptavidin (Fig. 8a, b).

Chain A of our Apo-SFX structure was captured in a closed-loop conformation with a continuous electron density of water molecules suggesting that those water molecules may be mimicking partially occupied biotin (Supplementary Fig. 15a). This is consistent with a previous study that had comparable results at chain A[46]. On the other hand, streptavidin–avidin affinity comes from a hydrophobic cage caused by a Van der Waals and hydrogen bond network associated with water molecules[15] (Figs. 5a–d and 7a–c). The intrinsic plasticity of L3/4 via cooperative allosteric effects of these residues may be the cause of an asymmetrical binding event of biotin. The polar interaction networks and number of coordinated water molecules in contact with streptavidin are directly related to the L3/4 conformation. It has a closed conformation through increased polar interactions at the binding site (Fig. 5a–d and Supplementary Fig. 15a). However, decreases in coordinated water molecules are associated with an open conformation of the loop, acting as a

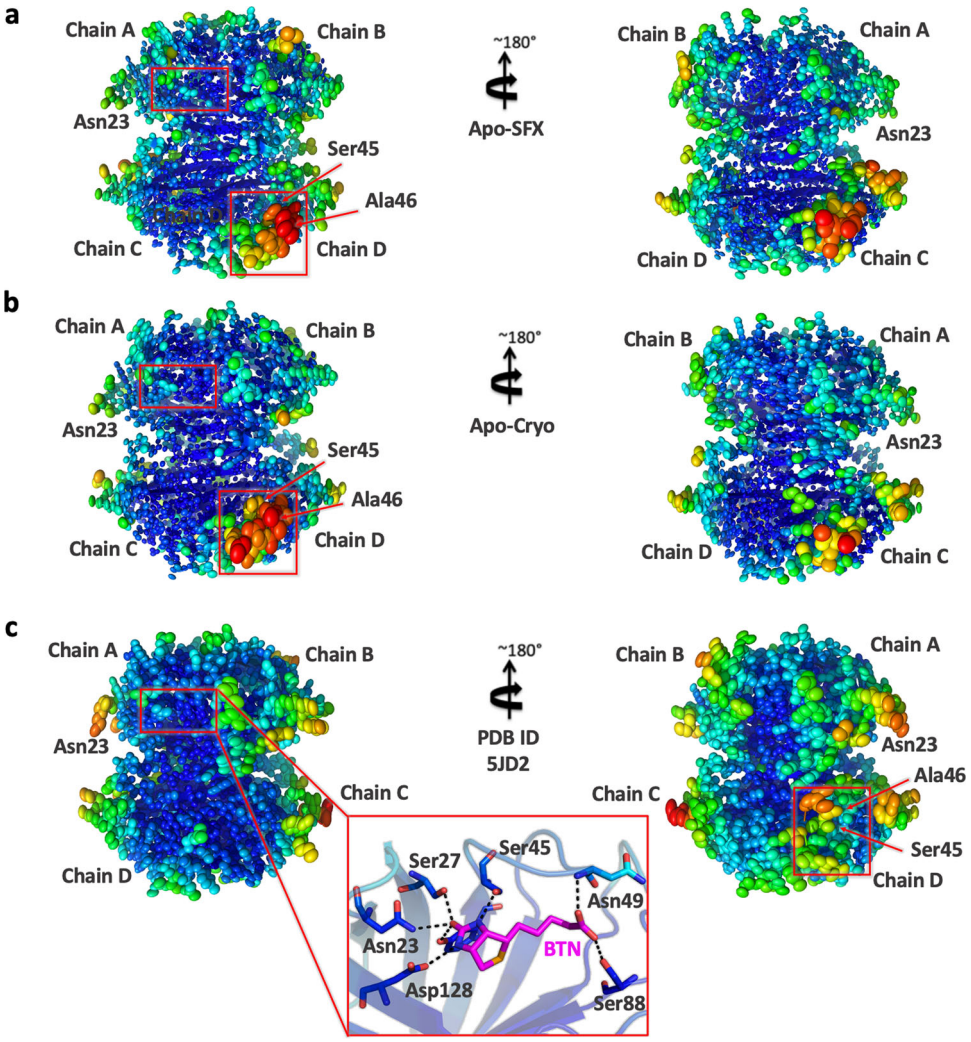

Fig. 6 Representation of thermal ellipsoid structures of streptavidin structures. a Apo-SFX structure of streptavidin, **b** Apo-Cryo structure of streptavidin, and (**c**) Holo-SFX streptavidin in complex with selenobiotin (PDB ID: 5JD2) are shown to determine the stability. Red boxes indicate flexible (red/orange) and stable (blue/green) regions on the streptavidin structures via *B*-factor presentation. The stable binding pocket of biotin is shown in **c**.

"lid" (Fig. 4a–c and Supplementary Fig. 15b–d). H-bond formation is a dynamic process[47] and these alternative extensive polar interaction networks of tetrameric streptavidin may contribute to the observed asymmetry. Similar to the Holo-SFX structure (Fig. 3a–d), Holo-CryoEM structure of streptavidin in complex with biotin (PDB ID: 6J6J) was superposed with our Apo-SFX structure (Supplementary Fig. 9a–d). The comparison of these structures suggests that the two techniques can capture alternative binding conformations and expand the conformational space sampling of the active site loop.

Previous studies described that L3/4 may or may not be randomly open in three monomers and closed in the last one. This open/closed loop conformation cannot be caused by crystal-packing interactions[46,48]. Our data suggest that this structural feature is intermolecular allostery between monomers of streptavidin. Recently, a new model was proposed to describe structural cooperativity of streptavidin and a cooperative allosterism upon binding biotin[23]. Ligand binding is characterized by L3/4. It functions as a "lid" that closes the binding pocket when it binds to biotin. In the Apo-SFX structure, L3/4 appears very flexible and unmodeled. However, our atomic-resolution structural data and GNM analysis suggest that there is a predisposed streptavidin cooperative allosterism not mediated by the first biotin molecule. Moreover, the open conformation of L3/4 is observed in three subunits while the fourth L3/4 region is observed in closed state, which is a harmonic motion that triggers the first biotin binding (Supplementary Figs. 16a–d and 17). The tetrameric structure of streptavidin provides higher affinity by water channels and "lid" like L3/4 movement caused by those cooperative and allosteric binding events. To determine and validate the accuracy of previous structures of streptavidin, the SFX approach offers structural data without temperature or radiation damage, providing a solid template for future studies. The next step to better understand the details of this binding and cooperative allosterism is performing time-resolved structural analysis by using ultrabright and ultrafast XFELs[49].

Methods

Sample preparation for SFX crystallography and cryo-synchrotron crystallography. Purchased core-streptavidin protein (Cat# Streptavidin-501; Creative Biomart, USA) was added into dithiothreitol solution with a 1 mM final concentration. Then streptavidin proteins were crystallized by sitting-drop microbatch screening under oil and using 72-well Terasaki crystallization plates. For crystallization, the protein was mixed with ~3500 commercially available sparse matrix crystallization screening conditions (1:1 ratio, v/v) at ambient temperature. The best crystals were grown in Pact Premier^{TM} 100 mM MMT buffer pH 6.0 and 25 % w/v PEG 1500 and were covered with 100% paraffin oil. Microcrystals 1–5 × 5–10 × 10–20 μm^3 in size were passed through 100 micron plastic mesh filters (Millipore, USA) in the same mother liquor composition to eliminate the large single crystals and other impurities before the data collection. Crystal concentration

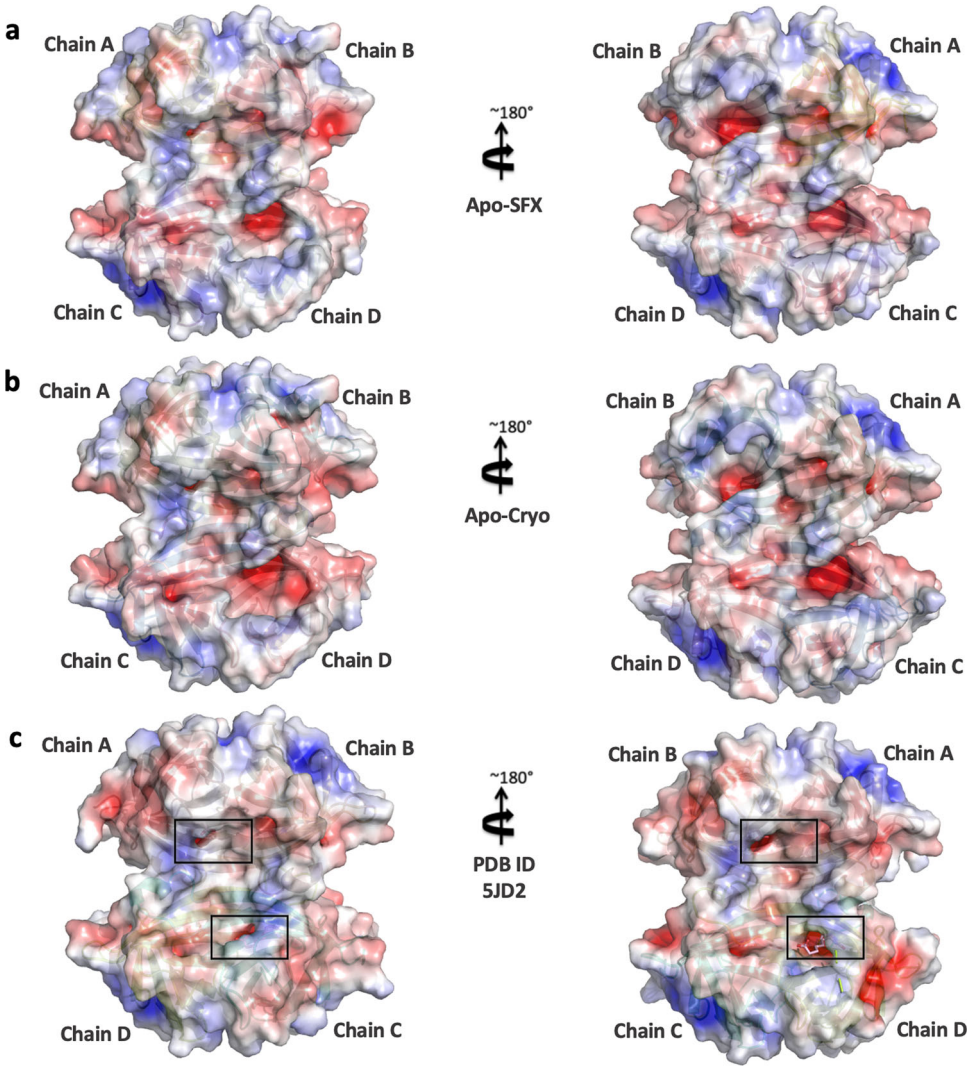

Fig. 7 Representation of electrostatic surfaces. a Apo-SFX structure of streptavidin, **b** Apo-Cryo structure of streptavidin, and **c** Holo-SFX streptavidin in complex with selenobiotin (PDB ID: 5JD2) are shown to detect the charge distribution. Holo-SFX structure is colored in light pink and shown with squares.

was detected as 10^{10}–10^{11} particles per ml for SFX based on light microscopy. Initial crystals of the batched crystalline slurry were not pretested for diffraction quality before XFEL and synchrotron beamtime. For a better comparison with GNM analysis, Holo-SFX crystals and Apo-SFX crystals were obtained from the same batch with minimized variables by using the same crystallization conditions, mother liquor and protein sample.

Transport of microcrystals for SFX studies at MFX instrument at the LCLS. Crystal slurry at the total volume of 1.9 ml was transferred to a 2 ml screw-top cryovial (Wuxi NEST Biotechnology, China cat#607001). These vials were wrapped loosely by Kimwipes (Kimberly-Clark, USA) and tightly placed in 20 ml screw top glass vials to provide insulation and prevent mechanical shocks during air transportation. The vials were wrapped with excess amounts of cotton (Ipek, Turkey) and placed in a Ziploc^{TM} bag (SC Johnson, USA) to provide both added layer of insulation and mechanical shock absorption. Furthermore, Ziploc^{TM} bags are placed into a styrofoam box, which was padded with ~1 kg of cotton and covered with an additional layer of 1 cm-thick loose cotton. Packing the samples with cotton, which prevented physical damage of the crystals, and the successful transportation to XFEL was followed by diffraction to 1.7 Å resolution.

Microfluidic Electrokinetic Sample Holder (MESH) sample injection of streptavidin crystals for SFX studies at MFX instrument at the LCLS. The 1.6 ml sample reservoir was loaded with streptavidin crystal slurry in their unaltered mother liquor as described above. The MESH injector was used for the injection of streptavidin crystals[50]. The sample capillary was a 200 µm ID × 360 µm OD × 1.0 m long fused silica capillary. The applied voltage on the sample liquid was typically 2500–3000 V, and the counter electrode was grounded. The sample flow rate was typically between 2.5 and 8 µl/min.

Data collection and analysis for SFX studies at LCLS. SFX data was collected during the LCLS beamtime (ID: mfxp17318) at the MFX instrument of LCLS at SLAC National Accelerator Laboratory (Menlo Park, CA). The radiation damage-free diffraction data collected from streptavidin microcrystals on a ePix10k2M pixel array detector installed at the MFX instrument. X-ray beam with a vertically polarized pulse with duration of 30 fs was focused using compound refractive beryllium lenses to a beam size of ~6 × 6 µm full width at half maximum at a pulse energy of 0.8 mJ, a photon energy of 9.8 keV (1.25 Å) and a repetition rate of 120 Hz. OM monitor[51] and *PSOCAKE*[52,53] were used to monitor crystal hit rates, analyze the gain switching modes, and determine the initial diffraction geometry of the detector[28]. The detector distance was arranged as 18 mm, with an achievable resolution of 2.1 Å at the edge of the detector and 1.64 Å at the corner of the detector. A total of 691,200 detector frames were collected continuously without any clogging issues from streptavidin microcrystals.

Data collection and analysis for cryo-synchrotron studies at SSRL. Synchrotron X-ray diffraction data were collected from a single crystal for apo-streptavidin with a Pilatus 6 M detector at microfocus beamline BL12-2 at the SSRL in Menlo Park, CA. The diffraction data in space group P21 were collected to 1.1 Å resolution with unit cell dimensions $a = 46.36$ Å, $b = 85.76$ Å, $c = 58.13$ Å; $\alpha = 90.00$, $\beta = 98.71$, $\gamma = 90.00$ at a wavelength of 0.979 Å and −180 °C.

Data processing for SFX and cryo-synchrotron structures: hit finding, indexing, and scaling. The diffraction data for the SFX structure were collected through the MFX instrument using ePix10k2M detector. Total diffraction patterns were selected as potential crystal hits using the *CHEETAH* software[54]. The hit finding, which is based on Bragg reflections, was performed by using peakfinder8 and the images containing >20 peaks were classified as crystal hits that were

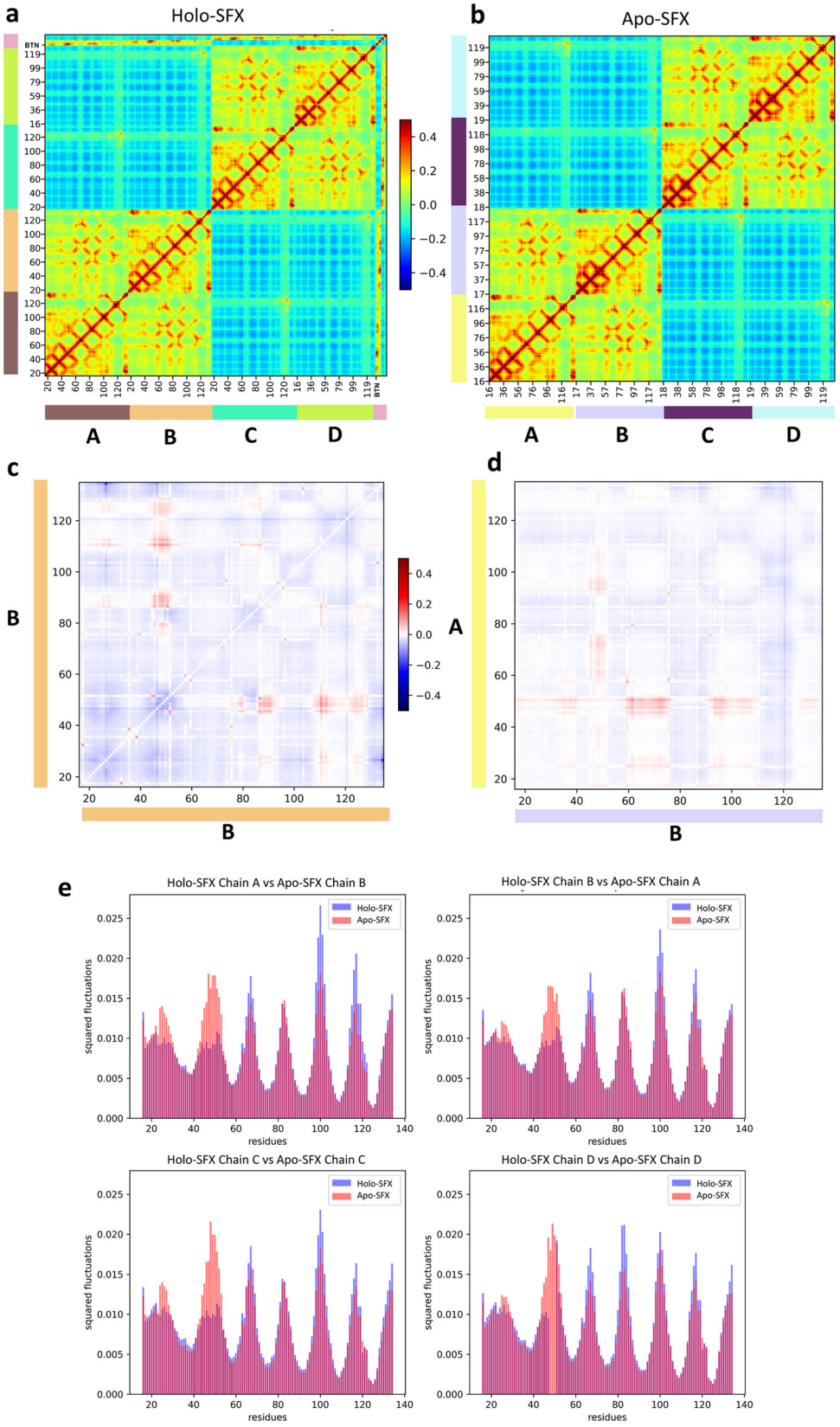

Fig. 8 Gaussian Network Model (GNM) analysis results for Apo-SFX and Holo-SFX (PDB ID: 5JD2) structures of streptavidin with selenobiotin. **a** Cross-correlation heat-map from overall GNM modes for Holo-SFX structure. Selenobiotin was indicated with "BTN" in the figure. **b** Apo-SFX structure GNM analysis heat-map results from overall modes. Highly correlated residue motion was represented with red and anti-correlated residue motions with blue color in **a**, **b**. **c** The differences between intrachain cross-correlations of chain B for Holo-SFX structure over Apo-SFX structure results. **d** Differences in the interchain cross-correlations of Holo-SFX structure over Apo-SFX structure at cross-sections of chains A and B. Differences in correlations are represented with blue color for decrease and red for increase. **e** Mean squared fluctuations of each chain of Holo-SFX structure and Apo-SFX structure was calculated from the 10 slowest mode from GNM analysis.

indexed by using the *CrystFEL* software package[55,56] version 9.0[57]. While *XGANDALF*[58], *DIRAX*[59], *MOSFLM*[60], and *XDS*[61] were used as indexing algorithms, the indexed reflections were subsequently integrated and merged using *PARTIALATOR*[62] applying the unity model over 3 iterations and the max-ADU set to 7500. The complete reflection intensity list from *CrystFEL* was then scaled and cut using the *TRUNCATE* program from the *CCP4* suite[63] prior to further processing. For streptavidin crystals, the final dataset included 384,250 hits with a total of 106,021 indexed patterns (28%) was merged into a final dataset ($P12_11$, unit cell: $a = 47.40$ Å, $b = 87.70$ Å, $c = 58.90$ Å; $\alpha = 90.00$, $\beta = 98.90$, $\gamma = 90.00$) (Table 1). Additionally, using a resolution cutoff at 1.7 Å, an R_{split} of 11.0% was obtained along with a CC* of 0.99 over the entire resolution range. The final dataset had an R_{split} of 77.8%, and CC* of 0.87 in the highest-resolution shell. For cryo-synchrotron structure, X-ray diffraction data ($P12_11$, unit cell: $a = 46.36$ Å, $b = 85.76$ Å, $c = 58.13$ Å; $\alpha = 90.00$, $\beta = 98.71$, $\gamma = 90.00$) were collected by using a Dectris Pilatus 6 M detector installed at BL-12-2 instrument at SSRL, which was processed with *XDS*[61] package for indexing and scaled by using *XSCALE*[61]. The resolution cutoff set to 1.1 Å without negatively impacting R_{free} and R_{work} (Table 1).

Structure determination and refinement of crystal structures. Apo-streptavidin structures, obtained at LCLS (MFX) and cryo-synchrotron at SSRL (BL12-2), were determined by using the automated molecular replacement program *PHASER*[64] implemented in the *PHENIX* software[65] with the previously published Holo-SFX structure as a search model and initial rigid-body refinement[43]. After a simulated-annealing refinement, individual coordinates and TLS parameters were refined. Potential positions of altered side chains and water molecules were checked by using the program *COOT*[66]. Then, positions with strong difference density were retained. The Ramachandran statistics for Apo-SFX structure (most favored/additionally allowed/disallowed) were 98.31/1.48/0.21%, respectively. The Ramachandran statistics for cryo-synchrotron structure (most favored/additionally allowed/disallowed) were 97.47/2.11/0.42%, respectively. For an understanding ligand-binding dynamics, Apo-SFX structure is aligned with the ambient temperature Holo-SFX structure[43] and figures were generated by the *PyMOL* software[67].

Temperature factor analysis and generation of ellipsoids. Both SFX and cryo-synchrotron structures were examined to generate ellipsoid structures based on *B*-factor. The generation of ellipsoid models via *PyMOL*[67] was enabled based on structure refinement with TLS parameters through *PHENIX*[68]. Later on, these two structures were compared with the Holo-SFX structure to provide better understanding of the flexibility of atoms, side chains, and domains. The all ellipsoid structures were colored with rainbow selection on *PyMOL*[67].

GNM analysis. Apo-SFX streptavidin and Holo-SFX streptavidin were analyzed by Normal Mode Analysis with GNM using *ProDy*[69]. Contact maps were defined with all Cα atoms of the proteins (residue numbers between 15 and135). The selenobiotin atoms N1, C2, C9, and O12 were included in the holo structure's GNM. Thus, the Apo-SFX streptavidin had 476 atoms selected to build a Kirchhoff matrix and the selenobiotin-bound structure had 486. Same cutoff distance of 7.3 Å was selected in both models to assume pairwise interactions. Default spring constant of 1.0 was used for both structures. All normal modes were calculated with GNM: 475 non-zero modes were obtained for the apo structure and 488 non-zero modes for the holo structure. The theoretical fluctuations calculated with all GNM modes were compared with the experimental *B*-factors. Cross-correlations between residue fluctuations were determined over all GNM modes as well. The differences in cross-correlations between Holo-SFX and Apo-SFX structures were calculated at selected sections: intrachain cross-correlations of chain A in Apo-SFX were subtracted from the intrachain cross-correlations of chain B in selenobiotin-bound structure; and the interchain cross-correlations between chains A and B were subtracted similarly. Their results are presented as heat-maps. The selections were decided after superposing the Apo-SFX and Holo-SFX structures: chain B of the apo-structure aligned with the chain A of the holo-structure. The yen slowest modes were chosen for analysis of the global motions based on their high variance calculated with *ProDy*. The weighted squared fluctuations of the two structures at these modes were aligned to compare the selenobiotin-bound and unbound state dynamics of streptavidin.

Reporting summary. Further information on research design is available in the Nature Research Reporting Summary linked to this article.

Data availability

Presented two apo-streptavidin in this article are available as 7EK8 and 7EK9 on the Protein Data Bank. Any remaining information can be obtained from the corresponding author upon reasonable request.

Received: 18 May 2021; Accepted: 28 October 2021;
Published online: 20 January 2022

References

1. Hendrickson, W. A. et al. Crystal structure of core streptavidin determined from multiwavelength anomalous diffraction of synchrotron radiation. *Proc. Natl Acad. Sci. USA* https://doi.org/10.1073/pnas.86.7.2190 (1989).
2. Lim, K. H., Huang, H., Pralle, A. & Park, S. Engineered streptavidin monomer and dimer with improved stability and function. *Biochemistry* https://doi.org/10.1021/bi2010366 (2011).
3. Freitag, S., Trong, I. L. E., Klumb, L., Stayton, P. S. & Stenkamp, R. E. Structural studies of the streptavidin binding loop. *Protein Sci.* https://doi.org/10.1002/pro.5560060604 (1997).
4. Bleuler-Martinez, S., Schmieder, S., Aebi, M. & Künzler, M. Biotin-binding proteins in the defense of mushrooms against predators and parasites. *Appl. Environ. Microbiol.* https://doi.org/10.1128/AEM.02286-12 (2012).
5. Wu, S. C., Ng, K. K. S. & Wong, S. L. Engineering monomeric streptavidin and its ligands with infinite affinity in binding but reversibility in interaction. *Proteins* https://doi.org/10.1002/prot.22446 (2009).
6. Taylor, C. R., Shi, S.-R. & Barr, N. J. in *Techniques of Immunohistochemistry* (ed. Dabbs, D. J.) Ch. 1 (Elsevier, 2011).
7. DeChancie, J. & Houk, K. N. The origins of femtomolar protein-ligand binding: hydrogen-bond cooperativity and desolvation energetics in the biotin-(strept)avidin binding site. *J. Am. Chem. Soc.* https://doi.org/10.1021/ja066950n (2007).
8. Miyamoto, S. & Kollman, P. A. Absolute and relative binding free energy calculations of the interaction of biotin and its analogs with streptavidin using molecular dynamics/free energy perturbation approaches. *Proteins* **16**, 226–245 (1993).
9. Miyamoto, S. & Kollman, P. A. What determines the strength of noncovalent association of ligands to proteins in aqueous solution? *Proc. Natl Acad. Sci. USA* **90**, 8402–8406 (1993).
10. Pazy, Y., Kulik, T., Bayer, E. A., Wilchek, M. & Livnah, O. Ligand exchange between proteins: exchange of biotin and biotin derivatives between avidin and streptavidin. *J. Biol. Chem.* https://doi.org/10.1074/jbc.M202874200 (2002).
11. Sano, T., Vajda, S., Smith, C. L. & Cantor, C. R. Engineering subunit association of multisubunit proteins: a dimeric streptavidin. *Proc. Natl Acad. Sci. USA* https://doi.org/10.1073/pnas.94.12.6153 (1997).
12. Kada, G., Kaiser, K., Falk, H. & Gruber, H. J. Rapid estimation of avidin and streptavidin by fluorescence quenching or fluorescence polarization. *Biochim. Biophys. Acta* https://doi.org/10.1016/S0304-4165(98)00177-9 (1999).
13. Dundas, C. M., Demonte, D. & Park, S. Streptavidin-biotin technology: Improvements and innovations in chemical and biological applications. *Appl. Microbiol. Biotechnol.* https://doi.org/10.1007/s00253-013-5232-z (2013).
14. Fairhead, M. et al. Love-Hate ligands for high resolution analysis of strain in ultra-stable protein/small molecule interaction. *Bioorg. Med. Chem.* https://doi.org/10.1016/j.bmc.2014.07.029 (2014).
15. Fairhead, M., Krndija, D., Lowe, E. D. & Howarth, M. Plug-and-play pairing via defined divalent streptavidins. *J. Mol. Biol.* https://doi.org/10.1016/j.jmb.2013.09.016 (2014).
16. Castner, D. G. & Ratner, B. D. in *Principles of Regenerative Medicine* (eds Atala, A., Lanza, R., Mikos, A. G. & Nerem, R.) Ch. 31 (Academic, 2019).
17. Zhang, M., Biswas, S., Deng, W. & Yu, H. The crystal structure of monovalent streptavidin. *Sci. Rep.* https://doi.org/10.1038/srep35915 (2016).
18. Hyre, D. E. Cooperative hydrogen bond interactions in the streptavidin-biotin system. *Protein Sci.* https://doi.org/10.1110/ps.051970306 (2006).
19. Sano, T., Pandori, M. W., Chen, X., Smith, C. L. & Cantor, C. R. Recombinant core streptavidins: a minimum-sized core streptavidin has enhanced structural stability and higher accessibility to biotinylated macromolecules. *J. Biol. Chem.* https://doi.org/10.1074/jbc.270.47.28204 (1995).
20. Jones, S. & Thornton, J. M. Protein-protein interactions: a review of protein dimer structures. *Prog. Biophys. Mol. Biol.* https://doi.org/10.1016/0079-6107(94)00008-W (1995).
21. Williams, P. A. et al. Crystal structure of human cytochrome P450 2C9 with bound warfarin. *Nature* https://doi.org/10.1038/nature01862 (2003).
22. González, M. et al. Interaction of biotin with streptavidin. Thermostability and conformational changes upon binding. *J. Biol. Chem.* https://doi.org/10.1074/jbc.272.17.11288 (1997).
23. Waner, M. J. et al. Streptavidin cooperative allosterism upon binding biotin observed by differential changes in intrinsic fluorescence. *Biochem. Biophys. Rep.* https://doi.org/10.1016/j.bbrep.2018.12.011 (2019).
24. Fischer, M. Macromolecular room temperature crystallography. *Q. Rev. Biophys.* **54**, e1 (2021).
25. Bradford, S. et al. Temperature artifacts in protein structures bias ligand-binding predictions. *Chem. Sci.* https://doi.org/10.1039/D1SC02751D (2021).
26. Fraser, J. S. et al. Accessing protein conformational ensembles using room-temperature X-ray crystallography. *Proc. Natl Acad. Sci. USA* https://doi.org/10.1073/pnas.1111325108 (2011).

27. Sierra, R. G. et al. The macromolecular femtosecond crystallography instrument at the Linac Coherent Light Source. *J. Synchrotron Radiat*. https://doi.org/10.1107/S1600577519001577 (2019).
28. Van Driel, T. B. et al. The ePix10k 2-megapixel hard X-ray detector at LCLS. *J. Synchrotron Radiat*. https://doi.org/10.1107/S1600577520004257 (2020).
29. Bahar, I. et al. Direct evaluation of thermal fluctuations in proteins using a single-parameter harmonic potential. *Folding Des*. https://doi.org/10.1016/S1359-0278(97)00024-2 (1997).
30. Stenkamp, R. et al. Structural studies of the streptavidin binding loop. *Protein Sci*. https://doi.org/10.1002/pro.5560060604 (1997).
31. Le Trong, I. et al. Streptavidin and its biotin complex at atomic resolution. *Acta Crystallogr. Sect. D Biol. Crystallogr*. https://doi.org/10.1107/S0907444911027806 (2011).
32. Reznik, G. O., Vajda, S., Cantor, C. R. & Sano, T. A streptavidin mutant useful for directed immobilization on solid surfaces. *Bioconjug. Chem*. https://doi.org/10.1021/bc015507t (2001).
33. Lecot, S., Chevolot, Y., Phaner-Goutorbe, M. & Yeromonahos, C. Impact of silane monolayers on the adsorption of streptavidin on silica and its subsequent interactions with biotin: molecular dynamics and steered molecular dynamics simulations. *J. Phys. Chem. B* https://doi.org/10.1021/acs.jpcb.0c04382 (2020).
34. Cong, Y. et al. Entropic effect and residue specific entropic contribution to the cooperativity in streptavidin-biotin binding. *Nanoscale* https://doi.org/10.1039/c9nr08380d (2020).
35. Baugh, L., Le Trong, I., Stayton, P. S., Stenkamp, R. E. & Lybrand, T. P. A streptavidin binding site mutation yields an unexpected result: an ionized Asp128 residue is not essential for strong biotin binding. *Biochemistry* https://doi.org/10.1021/acs.biochem.6b00698 (2016).
36. Bahar, I., & Rader, A. J. Coarse-grained normal mode analysis in structural biology. *Curr. Opin. Struct. Biol*. https://doi.org/10.1016/j.sbi.2005.08.007 (2005).
37. Bahar, I., Atilgan, A. R., Demirel, M. C. & Erman, B. Vibrational dynamics of folded proteins: significance of slow and fast motions in relation to function and stability. *Phys. Rev. Lett*. **80**, 2733–2736 (1998).
38. Farmer, T. B. & Caprioli, R. M. Determination of protein-protein interactions by matrix-assisted laser desorption/ionization mass spectrometry. *J. Mass Spectrom*. **33**, 697–704 (1998).
39. Price, N. C. in *Mechanisms of Protein Folding* (ed. Pain, R. H.) 160–193 (IRL Press, 1994).
40. Klotz, I. M., Langerman, N. R. & Darnall, D. W. Quaternary structure of proteins. *Annu. Rev. Biochem*. https://doi.org/10.1146/annurev.bi.39.070170.000325 (1970).
41. Yu, Z. et al. Allosteric coupling between α-rings of the 20S proteasome. *Nat. Commun*. https://doi.org/10.1038/s41467-020-18415-7 (2020).
42. Liu, F., Zhang, J. Z. H. & Mei, Y. The origin of the cooperativity in the streptavidin-biotin system: a computational investigation through molecular dynamics simulations. *Sci. Rep*. https://doi.org/10.1038/srep27190 (2016).
43. Hunter, M. S. et al. Selenium single-wavelength anomalous diffraction de novo phasing using an X-ray-free electron laser. *Nat. Commun*. https://doi.org/10.1038/ncomms13388 (2016).
44. Song, J., Li, Y., Ji, C. & Zhang, J. Z. H. Functional loop dynamics of the streptavidin-biotin complex. *Sci. Rep*. **5**, 1–10 (2015).
45. Le Trong, I., Humbert, N., Ward, T. R., & Stenkamp, R. E. Crystallographic analysis of a full-length streptavidin with its C-terminal polypeptide bound in the biotin binding site. *J. Mol. Biol*. https://doi.org/10.1016/j.jmb.2005.11.086 (2006).
46. Le Trong, I. et al. Streptavidin and its biotin complex at atomic resolution. *Acta Crystallogr. Sect. D Biol. Crystallogr*. https://doi.org/10.1107/S0907444911027806 (2011).
47. Panek, J. J., Ward, T. R., Jezierska-Mazzarello, A. & Novič, M. Flexibility of a biotinylated ligand in artificial metalloenzymes based on streptavidin-an insight from molecular dynamics simulations with classical and ab initio force fields. *J. Comput. Aided Mol. Des*. https://doi.org/10.1007/s10822-010-9369-x (2010).
48. Chivers, C. E., Koner, A. L., Lowe, E. D. & Howarth, M. How the biotin-streptavidin interaction was made even stronger: Investigation via crystallography and a chimaeric tetramer. *Biochem. J*. https://doi.org/10.1042/BJ20101593 (2011).
49. Neutze, R., & Moffat, K. Time-resolved structural studies at synchrotrons and X-ray free electron lasers: opportunities and challenges. *Curr. Opin. Struct. Biol*. https://doi.org/10.1016/j.sbi.2012.08.006 (2012).
50. Sierra, R. G. et al. Concentric-flow electrokinetic injector enables serial crystallography of ribosome and photosystem II. *Nat. Methods* https://doi.org/10.1038/nmeth.3667 (2015).
51. Mariani, V. et al. OnDA: online data analysis and feedback for serial X-ray imaging. *J. Appl. Crystallogr*. https://doi.org/10.1107/S1600576716007469 (2016).
52. Damiani, D. et al. Linac Coherent Light Source data analysis using psana. *J. Appl. Crystallogr*. https://doi.org/10.1107/S1600576716004349 (2016).
53. Thayer, J. et al. Data systems for the Linac coherent light source. *Adv. Struct. Chem. Imaging* https://doi.org/10.1186/s40679-016-0037-7 (2017).
54. Barty, A. et al. Cheetah: software for high-throughput reduction and analysis of serial femtosecond X-ray diffraction data. *J. Appl. Crystallogr*. https://doi.org/10.1107/S1600576714007626 (2014).
55. White, T. A. et al. CrystFEL: a software suite for snapshot serial crystallography. *J. Appl. Crystallogr*. https://doi.org/10.1107/S0021889812002312 (2012).
56. White, T. A. et al. Recent developments in CrystFEL. *J. Appl. Crystallogr*. https://doi.org/10.1107/S1600576716004751 (2016).
57. White, T. A. Processing serial crystallography data with crystFEL: a step-by-step guide. *Acta Crystallogr. Sect. D Struct. Biol*. https://doi.org/10.1107/S205979831801238X (2019).
58. Gevorkov, Y. et al. XGANDALF - extended gradient descent algorithm for lattice finding. *Acta Crystallogr. Sect. A Found. Adv*. https://doi.org/10.1107/S2053273319010593 (2019).
59. Duisenberg, A. J. M. Indexing in single-crystal diffractometry with an obstinate list of reflections. *J. Appl. Crystallogr*. https://doi.org/10.1107/S0021889891010634 (1992).
60. Powell, H. R., Johnson, O. & Leslie, A. G. W. Autoindexing diffraction images with iMosflm. *Acta Crystallogr. Sect. D Biol. Crystallogr*. https://doi.org/10.1107/S0907444912048524 (2013).
61. Kabsch, W. Integration, scaling, space-group assignment and post-refinement. *Acta Crystallogr. Sect. D Biol. Crystallogr*. https://doi.org/10.1107/S0907444909047374 (2010).
62. White, T. A. et al. Recent developments in CrystFEL. *J. Appl. Crystallogr*. https://doi.org/10.1107/S1600576716004751 (2016).
63. Winn, M. D. et al. Overview of the CCP4 suite and current developments. *Acta Crystallogr. Sect. D Biol. Crystallogr*. https://doi.org/10.1107/S0907444910045749 (2011).
64. McCoy, A. J. et al. Phaser crystallographic software. *J. Appl. Crystallogr*. https://doi.org/10.1107/S0021889807021206 (2007).
65. Adams, P. D. et al. PHENIX: a comprehensive Python-based system for macromolecular structure solution. *Acta Crystallogr. Sect. D Biol. Crystallogr*. https://doi.org/10.1107/S0907444909052925 (2010).
66. Emsley, P. & Cowtan, K. Coot: model-building tools for molecular graphics. *Acta Crystallogr. Sect. D Biol. Crystallogr*. https://doi.org/10.1107/S0907444904019158 (2004).
67. DeLano, W. L. The PyMOL Molecular Graphics System, Version 2.3 (Schrödinger LLC, 2020).
68. Zucker, F., Champ, P. C. & Merritt, E. A. Validation of crystallographic models containing TLS or other descriptions of anisotropy. *Acta Crystallogr. Sect. D Biol. Crystallogr*. https://doi.org/10.1107/S0907444910020421 (2010).
69. Bakan, A., Meireles, L. M. & Bahar, I. ProDy: protein dynamics inferred from theory and experiments. *Bioinformatics* https://doi.org/10.1093/bioinformatics/btr168 (2011).

Acknowledgements

Authors would like to dedicate this manuscript to the memory of John C. H. Spence and Dr. Nizar Turker. The authors gratefully acknowledge use of the services and facilities of the Koç University IsBank Infectious Disease Center (KUIS-CID). H.D. acknowledges support from National Science Foundation (NSF) Science and Technology Centers grant NSF-1231306 (Biology with X-ray Lasers, BioXFEL). H.D. would like to thank Michelle Young, Ritu Khurana, Lori Anne Love, and Tracy Chou for their invaluable support and discussions. This publication has been produced benefiting from the 2232 International Fellowship for Outstanding Researchers Program, the 2244 Industrial PhD Fellowship Program, and the 1001 Scientific and Technological Research Projects Funding Program of the Scientific and Technological Research Council of Turkey (TÜBİTAK) (Project Numbers: 118C270, 119C132 and 120Z520). However, the entire responsibility of the publication belongs to the owner of the publication. The financial support received from TÜBİTAK does not mean that the content of the publication is approved in a scientific sense by TÜBİTAK. Use of the Linac Coherent Light Source (LCLS), SLAC National Accelerator Laboratory is supported by the U.S. Department of Energy, Office of Science, Office of Basic Energy Sciences under Contract No. DE-AC02-76SF00515. C.D. acknowledges support from TÜBİTAK (Project No: 120Z594). The authors gratefully acknowledge use of the services and facilities of the Koç University Research Center for Translational Medicine (KUTTAM), funded by the Presidency of Turkey, Presidency of Strategy and Budget. The content is solely the responsibility of the authors and does not necessarily represent the official views of the Presidency of Strategy and Budget. Portions of this research were carried out at Stanford Synchrotron Light Source (SSRL) at the SLAC National Accelerator Laboratory. SSRL is supported by the U.S. Department of Energy (DOE), Office of Science, Office of Basic Energy Sciences (OBES) under Contract No. DE-AC02-76SF00515. The SSRL Structural Molecular Biology Program is supported by the DOE Office of Biological and Environmental Research and by the National Institutes of Health, National Institute of General Medical Sciences (NIGMS) (including P41GM103393).

Author contributions

H.D., C.D., F.B.E., and G.Y. prepared the samples. A. Batyuk, Z.S., F.P., C.H.Y., C.K., and R.G.S. performed the sample delivery and on-site data collection. H.D., C.D., E.A., B.Y., E.D., F.B.E., G.Y., S.B., E.H.D., B.H., M.L., M.H.S., M.S.H., A. Barty, V.M., Z.S., F.P., C.K., A.C., T.D., and R.G.S. performed the remote data collection. S.B., O.M.Y., A. Barty, A.T., G.K.K., Z.S., F.P., and C.H.Y. executed the data processing. Structures were refined by H.D. Data analyzed by H.D., E.A., B.Y., E.D., and M.E. The manuscript was prepared by H.D., E.A., B.Y., and E.D. with input from all the coauthors.

Competing interests

The authors declare no competing interests.

Additional information

Supplementary information The online version contains supplementary material available at https://doi.org/10.1038/s42003-021-02903-7.

Correspondence and requests for materials should be addressed to Hasan DeMirci.

Peer review information *Communications Biology* thanks Pohl Milón and the other anonymous reviewers for their contribution to the peer review of this work. Primary handling editors: Ingrid Span and Anam Akhtar. Peer reviewer reports are available.